

CHANDRA AND XMM-NEWTON OBSERVATIONS OF THE NUCLEUS OF CENTAURUS A

D. A. Evans¹, R. P. Kraft², D. M. Worrall¹, M. J. Hardcastle¹, C. Jones², W. R. Forman²,
S. S. Murray²

ABSTRACT

We present X-ray spectra of the nucleus of the nearby radio galaxy Centaurus A from observations with the *XMM-Newton* EPIC CCD cameras (two exposures separated by 12 months) and the *Chandra* HETGS. For the first time in an FRI type galaxy, we resolve fluorescent $K\alpha$ emission from cold, neutral, or near-neutral iron at 6.4 keV, with an rms line width of ~ 20 eV. The Fe line parameters observed are consistent with fluorescent emission from material at a large distance from the active galactic nucleus, either in the form of an absorber that nearly completely surrounds the central engine or a torus that lies predominantly out of the line of sight. Unresolved emission lines from neutral Si $K\alpha$ at 1.74 keV and neutral S $K\alpha$ at 2.30 keV are also detected. We find no evidence in the data for a previously reported 6.8 keV broadened Fe line. The continuum spectrum is well fitted with a combination of a heavily absorbed power-law component that we relate, using Bondi theory, to accretion phenomena in the form of a standard, geometrically thin, optically thick disk, and a second, less absorbed, power-law component that we associate with emission from the subparsec VLBI radio jet.

Subject headings: galaxies: active - galaxies: individual (Centaurus A, NGC 5128) - galaxies: jets - X-rays: galaxies

1. INTRODUCTION

Centaurus A (NGC 5128, Cen A) is the nearest ($d \sim 3.4$ Mpc, $1'' \sim 17$ pc) active galaxy to the Milky Way. It exhibits complex morphology on scales ranging from milliarcseconds to degrees on the sky, and shows a rich variety of structure across the electromagnetic spectrum. Optically, the host of Cen A is an elliptical galaxy with a large bisecting dust lane, which is

¹University of Bristol, Department of Physics, Tyndall Ave., Bristol BS8 1TL, UK

²Harvard-Smithsonian Center for Astrophysics, 60 Garden St., Cambridge, MA 02138, USA

believed to be evidence for a recent merger. Resolved X-ray emission from the predominantly one-sided kiloparsec-scale radio jet has been detected in detail with *Chandra* (Kraft et al. 2000, 2002; Hardcastle et al. 2003), and measurements of the X-ray hot gas environment of Cen A using *Chandra* and *XMM-Newton* have been reported by Karovska et al. (2002) and Kraft et al. (2003).

The nuclear X-ray continuum spectrum of Cen A is described by a highly absorbed power law, with a photon index $\Gamma \sim 1.7$ and absorbing column $\sim 10^{23}$ atoms cm^{-2} (e.g., Tucker et al. 1973; Mushotzky et al. 1978). Two popular interpretations for the origin of the continuum are (1) the emission is associated with accretion phenomena in or near a disk (e.g., Turner et al. 1997a) and (2) the observed emission is from synchrotron self-Compton upscattering of the subparsec scale radio jet to X-ray energies (e.g., Grindlay et al. 1975; Chiaberge et al. 2001). The high absorbing column might, for example, originate from a dusty torus surrounding the accretion disk (e.g., Woźniak et al. 1998), or material that surrounds (4π sr) the nucleus (e.g., Miyazaki et al. 1996).

Previous X-ray satellites have detected unresolved line emission at ~ 6.4 keV in Cen A, corresponding to $K\alpha$ fluorescence from neutral or near-neutral states of iron (e.g., Mushotzky et al. 1978). The detection of less prominent lines from neutral Mg, Si and S, has also been claimed (Sugizaki et al. 1997). *BeppoSAX* observations of Cen A, carried out between 1997 and 2000, found evidence for two separate Fe $K\alpha$ lines: one cold and narrow, with a centroid energy of 6.4 keV, and the other broad and variable, with a centroid energy of 6.8 keV (Grandi et al. 2003). The observations were used to argue in favor of a hot, geometrically thick, optically thin accretion flow surrounded by material with different opacities. However, it should be noted that the uncertainties associated with the parameters of the 6.8 keV line were considerable.

Nuclear X-ray spectra of other low-power radio galaxies are commonly described by a power-law continuum, absorbed by a wide range of column densities, together with one or more fluorescent emission lines. Typical examples are 3C66B (Hardcastle et al. 2000), M87 (Wilson & Yang 2002), NGC 6251 (Gliozzi et al. 2004) and NGC 4261 (Gliozzi et al. 2003). The physical origin of the continuum spectrum in these other low-power galaxies, as with Cen A, is still uncertain. Some of the soft nuclear X-ray emission may be associated with emission from the base of a jet (Worrall & Birkinshaw 1994; Canosa et al. 1999), and hard components have been interpreted as either due to accretion processes (e.g., Turner et al. 1997b; Gliozzi et al. 2004) or a jet. Bondi theory (Bondi 1952) may be applied to calculate the radiative efficiency, η_{Bondi} , of an accreting supermassive black hole. If the accretion process has $\eta_{\text{Bondi}} \sim 1\text{--}10\%$ (e.g., Gliozzi et al. 2004), it is likely that the accretion flow takes the form of a geometrically thin, optically thick disk (Shakura & Sunyaev 1973).

Alternatively, if the radiative efficiency is much less than the canonical value (e.g., Gliozzi et al. 2003), the accretion flow process may be fundamentally different, and might take the form of a geometrically thick disk (e.g., Narayan & Yi 1995).

In this paper, we present the results from two *XMM-Newton* EPIC observations and a *Chandra* HETGS observation of X-ray emission from the nucleus of Cen A. For the first time in an FRI type galaxy, we resolve the fluorescent iron $K\alpha$ line emission using *Chandra* HETGS and show that the observed line energy, equivalent width, and variability properties are consistent with emission from a region distant from the central black hole. We present a detailed analysis of the X-ray continuum spectrum, and demonstrate that a more complex model than a single powerlaw is necessary to explain adequately the observed emission at low energies. We find that a second, less absorbed, soft power-law component can explain the low-energy emission and is likely associated with X-ray emission from the subparsec-scale radio jet. We apply Bondi accretion theory to show that the hard continuum can be interpreted as originating from an accretion flow in the form of a standard, geometrically thin disk.

The recessional velocity of Cen A corresponds to a redshift of $z=0.0018$. Because of Cen A’s proximity and peculiar velocity, however, this redshift is not indicative of its distance. The distance to Cen A has been measured by a variety of techniques, and a range of values have been quoted in the literature. The most recent measurement places it at 3.84 ± 0.35 Mpc (Rejkuba 2004), somewhat farther than the value 3.4 ± 0.15 Mpc claimed by Israel (1998). We used this latter value in our five previous papers on X-ray observations of Cen A, and for consistency we have adopted it in this paper. None of our conclusions would be changed if we adopted the larger value; the only effect would be to increase all luminosities by $\sim 30\%$. All spectral fits include absorption through our Galaxy using $N_{\text{H,Gal}} = 7.69 \times 10^{20}$ atoms cm^{-2} (Dickey & Lockman 1990). When comparing Cen A with other objects at cosmological distances, we use a cosmology in which $\Omega_m = 0.3$ and $\Omega_\Lambda = 0.7$, and we adopt $H_0 = 70 \text{ km s}^{-1} \text{ Mpc}^{-1}$.

2. OBSERVATIONS AND ANALYSIS METHODS

2.1. XMM-Newton EPIC

Cen A was observed twice with the *XMM-Newton* EPIC instrument, on 2001 February 2 (~ 23 ks exposure) and 2002 February 6 (~ 13 ks exposure). In both observations the three EPIC CCD cameras (MOS1, MOS2, and pn) were operated with the medium optical blocking filter in place. The MOS cameras were operated in full-frame mode, and the pn

camera in extended full-frame mode. The results presented here were obtained using the latest software and calibration files available from the *XMM-Newton* project, SAS version 5.4.1. Calibrated event files were generated using the EMCHAIN and EPCHAIN scripts.

To check for intervals of high particle background, light curves were extracted for the whole field of view, excluding a $100''$ radius circle centered on the source. The events were filtered to include only those with PATTERN=0 and FLAG=0 attributes and for an energy range of 10–12 keV for the MOS cameras and 12–14 keV for the pn, where the particle background should dominate the emission. The light curves showed that there were no times of high background, which we defined following De Filippis et al. (2003) as more than 15 counts per 100 s time bin for the MOS1 and MOS2 cameras and more than 25 counts per 100 s time bin for the pn camera. For our analyses we measure background locally from large circles away from the source. A co-added MOS1, MOS2, and pn image of the second *XMM-Newton* observation is shown in Figure 1 with the area chosen for background subtraction marked.

The *XMM-Newton* observations of the nucleus of Cen A are heavily piled-up. We demonstrate this using two independent methods. First, we determined the count rates in a $100''$ source-centered circle with no PATTERN or FLAG filtering. As a representative case, the count rates in the second *XMM-Newton* observation were found to be 4.03 and 15.37 counts s^{-1} for the for the MOS1 and pn cameras, respectively. The maximum recommended count rates to avoid significant pileup are 0.70 and 3 counts s^{-1} for the MOS1 and pn cameras, respectively (Ehle et al. 2003). As a second independent estimate, we followed the prescription of Molendi & Sembay (2003) to produce an image of diagonal bipixels in the MOS cameras (assigned PATTERN numbers 26–29), which are produced almost solely by the pileup of two single-pixel events. We computed the ratio of number of diagonal bipixel events within a source-centered circle of radius $20''$ to that within an annulus of radii $20''$ and $50''$. For the second *XMM-Newton* observation, this ratio was found to be 32 ± 12 . The nominal ratio for unpiled up data is ~ 2.4 . The large excess of diagonal bipixel events in the central $20''$ demonstrates that this region is strongly affected by pileup. This method works only for the MOS cameras; for the pn camera, an image filtered with the FLAG = XMMEA_0 parameter was produced for energies ≤ 10 keV. This filtering parameter applies to events with a pattern that cannot be produced by a single photon i.e., those predominantly produced by pileup. This analysis shows for the pn camera that pileup is insignificant outside a source-centered circle of radius $20''$ (see Fig. 2).

In order to avoid complications due to pileup, we used an annulus for the spectral extraction region, thereby sampling the wings of the PSF and excluding the most heavily piled-up region. From the analysis described in the preceding paragraph, the inner radius

of the annulus was chosen to be $20''$. In determining the outer radius, there is a trade-off between the number of nuclear counts and the amount of underlying thermal galactic emission (not the focus of this investigation). We adopted $50''$, as a further increase in outer extraction radius would mean that we begin to sample knot B of the northeast kiloparsec-scale jet, and point sources to the southwest. To further minimize the effect of pileup, the event tables were filtered to include only events with the $\text{FLAG} = 0$ and $\text{PATTERN} = 0$ parameters. Redistribution matrix files (RMFs) and ancillary response files (ARFs) were generated using the SAS tasks *rmfgen* and *arfgen*. The ARF-generation corrects for the energy-dependent fraction of the PSF counts included in the annulus, parameterized by a King model (Ghizzardi et al. 2001a,b).

In our *XMM-Newton* analysis, the $20'' - 50''$ annulus contains both extended emission from the jet and hot gas and pointlike emission from the core in which we are interested here. To measure the spectrum of the nucleus alone, we used *Chandra*/ACIS-I data (observation date 2000 May 17; Kraft et al. 2001) to model spectrally the contribution from the extended components in the $20'' - 50''$ annulus. This emission was treated as an additional background in the *XMM-Newton* data by subtracting it from the *XMM-Newton* spectra. We used the appropriate ARFs for pointlike and extended emission in our analysis.

2.2. Chandra HETGS

The nucleus of Cen A was observed twice 2 weeks apart with the *Chandra* HETGS; first on 2001 May 9 and again on 2001 May 21. The live times of the two observations were 46.8 and 51.5 ks, respectively. Both observations were roll-constrained so that the jet was placed along the cross-dispersion direction to avoid contamination of the dispersed spectrum of the nucleus. The data were examined for periods of high background, and none were found. The nuclear spectra were extracted and grating ARFs and RMFs were created for both the HEG and the MEG data using the CIAO software package. Initially the two datasets were analyzed separately to search for temporal variability in either line or continuum features on the scale of weeks separating the two observations. No statistically significant differences were found, so the two datasets were combined, yielding a total observation time of 98.3 ks. Background was determined from a region offset from the dispersed spectra beyond the extraction region. Contamination of the nuclear spectrum from the other X-ray emitting components present in Cen A, including the hot gas and the X-ray binary population, was generally negligible for two reasons. First, the nuclear flux dominates the X-ray emission from the galaxy, and its spectrum is heavily absorbed ($N_{\text{H}} > 10^{23}$ atoms cm^{-2}), whereas the spectra of the other components are much softer and orders of magnitude less luminous. Second, the event

processing/order sorting algorithm used to extract grating spectra efficiently removed the contribution from these other components unless they are located within a few arcseconds of the core.

3. THE X-RAY SPECTRUM

3.1. Continuum Spectrum

3.1.1. *XMM-Newton EPIC*

The *XMM-Newton* spectral fitting was performed jointly for the MOS1, MOS2, and pn cameras for an energy range of 1.5–8 keV for each of the two observations, so as to avoid the low energies where thermal emission dominates the spectrum, as indicated by *Chandra*/ACIS imaging data. The net counts (1.5–8 keV) in our spectral fits to data from the annular extraction regions for the first and second observations, respectively, are MOS1: 11,773, 6,953; MOS2: 11,726, 7,086; pn: 21,251, 10,811. The data were grouped to 100 counts per PHA bin.

We initially modeled the nuclear continuum spectrum with a single, heavily-absorbed power-law. The normalizations of all spectral components were kept free for each camera. An Fe K α emission line at ~ 6.4 keV was included and modeled with a Gaussian function, and is discussed in detail in §3.2. The fit was poor; for example, for the second observation, $\chi^2 = 393$ for 207 dof, with large contributions to χ^2 at low energies (see Fig. 3). A substantial improvement in the fit was achieved by adding a second power-law component to the model (for example, for the second *XMM-Newton* observation, $\chi^2 = 211$ for 203 dof). The spectral parameters for the second power law are poorly constrained, so we decided to fix its photon index to 2. The best-fit spectral parameters for this model, together with 90% confidence errors for one interesting parameter ($\chi^2_{\min} + 2.7$), are given in Table 1 for both *XMM-Newton* observations. An unfolded spectrum for each *XMM-Newton* observation is given in Figure 5.

When estimating the parameters of the second power law we must take into account the statistical uncertainties in the model parameters for the resolved emission from jet and gas measured with *Chandra*. This was achieved by using maximum and minimum amounts of this emission, as described by 90% confidence limits. Using these upper and lower limits, we plot 90% confidence contours for the second power law for the MOS1 and pn cameras in Figure 4 for the first *XMM-Newton* observation. Results for the MOS2 are consistent with those for the MOS1, as are those for the first and second observations. We also estimate how

systematic errors in the *Chandra* annulus subtraction might affect the results of the second power law measured with *XMM-Newton*. A systematic error approaching a factor of 2 was required before any significant change in second power law properties was measured, within the uncertainties.

We independently confirmed the existence of the second power law component by analyzing data from the *Chandra* ACIS-I frame transfer streak. As can be seen from the *XMM-Newton* best-fitting unfolded spectrum in Figure 5, in the energy range 1.7–2.2 keV there is only a small contribution to the flux from the heavily absorbed primary power law. In this energy range, we measure a second power law flux of $\sim(8 \pm 4) \times 10^{-13}$ ergs cm $^{-2}$ s $^{-1}$ (90% confidence). The ACIS frame transfer streak in the same energy range should contain a similar flux and, crucially, does not contain a contribution from the kiloparsec-scale jet (which, if modelled incorrectly, could have affected the measured *XMM-Newton* core flux). Following Marshall et al. (2004), we determined the number of counts in the frame transfer streak using a rectangular extraction region surrounding the streak, using background determined from an adjacent region devoid of point sources. The rectangle was wide enough that $> 95\%$ of the source flux in the streak at any point was included. To determine the number of source events that occurred in the frame transfer streak, we scaled the number of counts measured from the core spectrum flux by the ratio of the pixel exposure time to the frame transfer time. We compared the measured 1.7–2.2 keV count rate in the ACIS-I frame transfer streak $[(1.34 \pm 0.19) \times 10^{-3}$ counts s $^{-1}$] with that expected for an absorbed power law with a flux of $(8 \pm 4) \times 10^{-13}$ ergs cm $^{-2}$ s $^{-1}$ $[(1.23 \pm 0.62) \times 10^{-3}$ counts s $^{-1}$], and found the two to be consistent.

The normalization of the pn camera was lower than that of the MOS cameras for the second power-law component in both *XMM-Newton* observations. The trend for the pn normalization to be low was also apparent (although not statistically significant) in the first power-law component (see Table 1). We attribute this discrepancy to remaining uncertainties in the calibration between the MOS and pn cameras.

Since we cannot rule out the possibility that the two power-law indices are the same, we tested a partial covering model in which a certain fraction of the emission is covered by an absorbing column $N_{\text{H},1} + N_{\text{H},2}$ and the remainder by an absorbing column $N_{\text{H},2}$. A Gaussian Fe emission line was included in the fit. This yielded an acceptable fit, for example, for the second *XMM-Newton* observation, $\chi^2 = 215$ for 205 dof. The counts spectrum and best-fitting model, together with contributions to χ^2 is shown in Figure 6 for the pn camera. These best-fitting spectral parameters for both *XMM-Newton* observations are given in Table 2.

3.1.2. *Chandra* HETGS

The *Chandra* spectral fitting was performed jointly for the high-energy grating (HEG) and medium-energy grating (MEG), over an energy range of 1.8–7 keV. The net counts in this energy range are 65,804 in the MEG and 68,400 in the HEG. The data were grouped to 100 counts per bin. A model containing a single, absorbed power law and an Fe K α line yielded an acceptable fit ($\chi^2 = 469$ for 528 dof). An initial analysis showed that the HEG and MEG normalizations agreed, so the normalizations of all spectral components were kept linked across the gratings. A detailed analysis of the line emission features is given in §3.2.

Guided by the inadequacy of a single, absorbed power-law fit to the *XMM-Newton* data, we explored the possible range of parameter values that a second power-law component could take in the *Chandra* data, despite the relative insensitivity compared to *XMM-Newton* in the energy range where this component is prominent. An improvement in the fit ($\Delta\chi^2 = 4.31$ for one additional parameter) was obtained by adding such a component with a frozen photon index of 2 and an absorption of 3.8×10^{22} atoms cm^{-2} , corresponding to the parameters of the second power-law in §3.1.1. The 90% confidence upper limit of the 1 keV normalization is $\sim 3 \times 10^{-3}$ photons $\text{cm}^{-2} \text{ s}^{-1} \text{ keV}^{-1}$, which is consistent with the *XMM-Newton* data. A counts spectrum is shown in Figure 7. The best-fit spectral parameters, together with 90% confidence errors for one interesting parameter ($\chi^2_{\text{min}} + 2.7$), are given in Table 1. This shows that the *Chandra* and *XMM-Newton* spectra are consistent.

3.2. Emission Lines

3.2.1. *Chandra* HETGS

We used the *Chandra* HETGS data at full resolution to study narrow emission line features. A heavily absorbed power law was jointly fitted to each data set for energy ranges of 4.0–6.0 keV and 7.2–8.0 keV, and the interpolated continuum subtracted from the data in the energy range 6.0–7.2 keV. The continuum parameters were consistent with those found in §3.1.

Neutral Fe K α and K β emission lines were fitted to the data and checked using an *F*-test for their statistical significance. The ratio of the intensities of the K α and K β lines was fixed to 150/17 when considering models containing both lines. In order to correctly evaluate any Fe K α line broadening, we modeled this emission as a doublet, with the energy difference between the K α_1 and K α_2 lines fixed at 13 eV (Bearden 1967), the intensity of the K α_2 line half of the K α_1 line, and made the line widths vary with each other. The addition of an Fe

$K\alpha$ line was highly significant ($\Delta\chi^2 = 90$ for three additional parameters). The Fe $K\alpha_1$ line had a measured centroid of 6.404 ± 0.006 keV and was found to be broadened, with a width of 20 ± 10 eV (90% confidence). The addition of an Fe $K\beta$ line was found to be statistically insignificant.

We also attempted to detect the broad 6.8 keV ionized iron line in the data, as claimed by Grandi et al. (2003) based on *BeppoSAX* observations. We found an insignificant improvement in the fit ($\Delta\chi^2 = 0.38$ for two additional parameters) with the inclusion of this line. Further, the best-fitting intensity of this line was consistent with zero. Parameter values are given in Table 3, and a counts spectrum showing the contributions of the Fe $K\alpha_1$ and $K\alpha_2$ lines is presented in Figure 8.

In addition, we searched for low-energy emission lines using MEG-1 data grouped to 15 counts per energy bin. The inclusion of a Si $K\alpha$ line at 1.74 keV was significant at $> 99.9\%$ on an F -test. We also found a significant improvement in the fit upon adding a S $K\alpha$ line at 2.30 keV. A counts spectrum showing the contributions of Si and S is shown in Figure 9, and parameter values are given in Table 3.

3.2.2. *XMM-Newton EPIC*

The *XMM-Newton* data were used to study the Fe line emission, but not contributions from Si and S, because of the lower energy resolution of *XMM-Newton* EPIC compared to *Chandra* HETGS. We examined data from the *XMM-Newton* RGS camera, but found that they had an insufficient signal-to-noise ratio to perform a useful analysis. We used the pn camera only for the *XMM-Newton* analysis, because of its larger effective area and better statistics as compared with either the MOS1 or MOS2 cameras. The method of continuum subtraction and analysis described in §3.2.1 was followed throughout. The residuals for the two *XMM-Newton* observations are shown overlaid in Figure 10. The line widths of all emission lines models were frozen to be narrow in *XSPEC*, with $\sigma = 10$ eV (small compared with the ~ 130 eV FWHM resolution of the EPIC pn camera at 6.4 keV).

The inclusion of an Fe $K\alpha$ line was statistically significant at greater than 99.9% on an F -test. The 90% confidence lower limit on the line centroids for each observation are 6.408 keV and 6.413 keV, marginally inconsistent with the centroid of 6.404 keV, measured with *Chandra* HETGS. This may be interpreted as due to a systematic error in the calibration of the energy scale of the pn camera, causing the line centroid to be apparently shifted to a slightly higher energy. This effect has been mentioned elsewhere (e.g., Worrall & Birkinshaw 2003). The line energy, line width, equivalent width, and unabsorbed flux of the Fe $K\alpha$ line

for both *XMM-Newton* observations are given in Table 3. There is no statistically significant evidence for an Fe K β line in the data.

We also searched for a broad, ionized emission line in the data by following the method used in the *Chandra* analysis. We found no statistically significant evidence for a blue tail to the Fe K α emission between an observed energy of 6.5 and 7.2 keV (see Fig. 10), unlike that reported in Grandi et al. (2003). Following the method of Grandi et al. (2003), we found no evidence in the data for a ~ 6.8 keV line and, when the parameters of the line were set to equal those in Grandi et al. (2003), we found a worse fit ($\Delta\chi^2 = 4.73$). When the intensity of the line was set to the 90% confidence lower limit in Grandi et al. (2003), the fit was still worse ($\Delta\chi^2 = 1.22$).

4. SOURCE VARIABILITY

X-ray light curves were created using the pn camera for each *XMM-Newton* observation using a source-centered circular extraction region with a radius 30". Background subtraction was applied using a source-centered annular extraction region of inner radius 400" and outer radius 600". To examine any variability of the hard, absorbed power law, an energy range of 3–10 keV was used. An energy range of 0.5–2.5 keV was also used to search for variability of the softer, second power-law component. Only events with FLAG = 0 and PATTERN = 0 parameters were selected.

To search for any intra-observation variability, the data were binned in time intervals of 500, 1000, and 2,000 seconds, and a χ^2 analysis used to test the null hypothesis. We found no significant intra-observation variability, with typical values of $P_{\chi^2} > 50\%$. In addition, we calculated the fluxes from the *XMM-Newton* and *Chandra* count rates in the energy band 4–7 keV: i.e., where the heavily-absorbed power law is likely to dominate and where there is reasonable effective area in both instruments. The *XMM-Newton* fluxes were calculated from 20" to 50" source-centered annular extraction regions in the pn camera data for both observations. The *Chandra* fluxes were found using the HEG+1 data. The results are given in Table 4. Because of the high count rate, the statistical errors were small. We found an increase in the 4–7 keV unabsorbed flux of $\sim 19\%$ between the two *XMM-Newton* observations, and a $\sim 57\%$ increase between the first *XMM-Newton* observation and the *Chandra* observation, similar in magnitude to the 60% variations previously reported (Benlloch et al. 2001). We also note that the 0.5–2.5 keV count rate increased by $\sim 48\%$ between the two *XMM-Newton* observations. Finally, we found that the Fe K α flux did not appear to correlate with the 4–7 keV continuum flux, as shown in Figure 11, and that any Fe K α flux variability was not statistically significant.

5. INTERPRETATION

5.1. Continuum

The nuclear spectrum of Cen A is well described by a two-component power-law model, with emission lines from Si, S, and Fe. This result is consistent with two distinct models of the active galactic nucleus geometry. The first (Turner et al. 1997a) is that $\sim 90\%$ of the nucleus of Cen A is covered by an absorbing column of $\sim (1.1\text{--}1.4) \times 10^{23}$ atoms cm^{-2} and $\sim 10\%$ by a column of $\sim (4.4\text{--}4.5) \times 10^{22}$ atoms cm^{-2} . This partial covering model gives the required low energy flux. A second possible interpretation of the data is that we are observing unresolved X-ray emission from two power-law components, each with some degree of intrinsic absorption. The second, less-absorbed component may be consistent with arising from the subparsec radio VLBI jet. High-resolution VLBI observations of Cen A (Tingay et al. 1998) have revealed a variety of radio structures, including a compact, self-absorbed core with a highly inverted spectrum and a subparsec-scale jet, extending to ~ 40 mas (0.7 pc). Emission from the core does not dominate over that from the jet in the VLBI observations, even at 8.4 GHz, where it is most prominent. At 4.8 GHz the flux is dominated by emission from the jet. We also note from Tingay et al. (1998) that radio variability by a factor of ~ 3 occurs in the self-absorbed core, and $\sim 70\%$ in the subparsec-scale jet, both on timescales of years.

Using a normalization of $\sim 5 \times 10^{-3}$ photons $\text{cm}^{-2} \text{ s}^{-1} \text{ keV}^{-1}$ (i.e. comparable to both the *XMM-Newton* and *Chandra* spectral fits) we calculate the flux density ratio of the 1 keV second power law X-ray emission and the parsec-scale jet seen in VLBI observations (Tingay et al. 1998). We perform a similar calculation with the kiloparsec-scale jet, using *Chandra*/ACIS-I observations (Kraft et al. 2002) and 8.4 GHz VLA observations (Hardcastle et al. 2003) in a source-centered $20''\text{--}50''$ annulus. The fluxes of each component, together with their ratios are given in Table 5. We find the X-ray to radio flux ratio for the VLBI jet and the second X-ray power-law component to be similar to that from the kiloparsec-scale jet emission detected with the *Chandra* CCDs and the VLA radio observations, which might imply a synchrotron origin for this unresolved X-ray emission.

Previous studies of the X-ray and radio flux properties of the active nuclei of low-power radio galaxies (Fabbiano et al. 1984; Worrall & Birkinshaw 1994; Canosa et al. 1999; Hardcastle & Worrall 1999) have shown a correlation between the luminosities of soft, unresolved X-ray emission and 5 GHz core radio emission. Figure 12 shows that the measured X-ray luminosity of the second power law detected in Cen A lies on or near the trendline established for the large B2 sample of radio galaxy cores (Canosa et al. 1999). This is consistent with the hypothesis that the observed low-energy X-ray emission originates from

the subparsec-scale VLBI jet.

5.2. Emission Lines

The measured line energy and width of the Fe $K\alpha$ line, together with its lack of response to continuum variations implies an origin in cool, neutral or near-neutral material far from the central black hole. This hypothesis is supported by the detection of unresolved emission lines from neutral Si and S. The measured Fe $K\alpha$ line width and the estimated black hole mass of $2 \times 10^8 M_\odot$ (Marconi et al. 2001) give an Fe emission radius of 0.1 pc (6 mas) using Keplerian arguments. Note that this value of M_{BH} is higher than the values presented in Israel (1998). Two models have previously been proposed to explain the possible geometry of the fluorescent region being illuminated by a primary power-law continuum. In the first model (Miyazaki et al. 1996), the emission arises from a cold cloud with an absorbing column of $\sim 10^{23}$ atoms cm^{-2} that entirely surrounds the nucleus. The predicted equivalent width of $\sim 60\text{--}70$ eV in this model is roughly consistent with that measured here. In the second model (Woźniak et al. 1998), the central engine is surrounded by a structure with an intrinsic absorption of $\gg 10^{23}$ atoms cm^{-2} that lies predominantly outside of the line of sight, such as a torus. The data presented here cannot distinguish between the two models, although it seems that line emission originating predominantly from the inner regions of an accretion disk is unlikely. In addition, the lack of observed line emission at higher energies (~ 6.7 keV) disfavors a model in which ionized species of Fe in an accretion disk close to the central black hole emit fluorescent lines. However, our results are consistent with a model in which a standard accretion disk emitting a fluorescent line at 6.4 keV is truncated and replaced by a hot radiatively inefficient accretion flow in the inner regions near the central engine, as discussed for NGC 4258 by, for example, Gammie, Narayan, & Blandford (1999) and Reynolds et al. (2000).

5.3. Nature of the accretion flow

We estimate the rate, \dot{M}_{Bondi} , at which the central black hole in Cen A gravitationally captures gas by applying Bondi accretion theory (Bondi 1952), and calculate the Bondi radiation efficiency, η_{Bondi} , by comparing the measured X-ray luminosity, L_X , with the Bondi luminosity, $\dot{M}_{\text{Bondi}}c^2$. The Bondi accretion rate may be written as

$$\dot{M}_{\text{Bondi}} = 4\pi R_A^2 \rho_A c_s, \tag{1}$$

where the accretion radius, R_A , is given by $R_A \simeq GM/c_s^2$, with ρ_A the density of gas at R_A , and c_s the sound speed.

We follow previous work in assuming that the gas supply for the central black hole is the X-ray-emitting hot gas, with a typical temperature of 0.5 keV. It should be noted that there are large amounts of cold, dense gas in the center of Cen A, so the Bondi accretion rate calculated here is a lower limit. We take the black hole mass to be $2 \times 10^8 M_\odot$, based on Very large Telescope infrared spectroscopy measurements of Cen A (Marconi et al. 2001). This gives a maximum accretion radius of 26 pc from the central black hole. At this radius, we take the gas density to be the interpolated central value of $3.7 \times 10^{-2} \text{ cm}^{-3}$ (Kraft et al. 2003), which is uncertain by factors of a few, and find $\dot{M}_{\text{Bondi}} = 6.41 \times 10^{-4} M_\odot \text{ yr}^{-1}$.

The 2–10 keV luminosity found with these observations of Cen A is $\sim 5 \times 10^{41} \text{ ergs s}^{-1}$. If Cen A accretes at the Bondi rate, we compare this measured X-ray luminosity with $\dot{M}_{\text{Bondi}} c^2$, to find an upper limit to the Bondi efficiency, $\eta_{\text{Bondi}} \sim 0.2\%$. In Table 6, we compare η_{Bondi} for Cen A with other galaxies (Quataert 2003; Baganoff et al. 2003; Loewenstein et al. 2001; Di Matteo et al. 2003; Gliozzi et al. 2003, 2004).

From Table 6, Cen A has an efficiency η_{Bondi} that is several orders of magnitude higher than other galaxies that have been interpreted to have a radiatively inefficient accretion flow, though it is somewhat smaller than the canonical efficiency of 1–10%. Taking this at face value, we favor either a standard, efficient, geometrically thin, optically thick disk for the accretion system in Cen A, or a hybrid model in which a radiatively inefficient optically thin inner accretion flow is surrounded by a standard thin disk (e.g., Narayan, McClintock, & Yi 1996). We finally note that η_{Bondi} for Cen A and the other sources in Table 6 is an upper limit, as we have ignored any role that cold gas might have in accreting onto the black hole. We also cannot be certain of the true value of M_{BH} .

6. CONCLUSIONS

We have presented results from one *Chandra* HETGS and two *XMM-Newton* EPIC observations of the nucleus of the nearby radio galaxy Centaurus A. We find that:

1. Resolved Fe $K\alpha$ line emission at 6.4 keV is detected with *Chandra*, with an rms line width of $\sim 20 \pm 10 \text{ eV}$ (90% confidence). The measured line energy of the Fe $K\alpha$ line, together with its narrowness and lack of response to continuum variations suggests an origin in cool, neutral or near-neutral material far from the central black hole. It is possible that this material takes the form of either an absorber that almost entirely

surrounds the central engine or a torus that lies predominantly out of the line of sight. However, we cannot rule out a contribution to the line emission from the outer parts of an accretion disk. Fluorescent $K\alpha$ emission from neutral Si at 1.74 keV and neutral S at 2.30 keV are also detected.

2. The hard (3–10 keV) X-ray spectrum is well-fitted by a heavily absorbed power-law model with a column density of $\sim 10^{23}$ atoms cm^{-2} and a photon index of ~ 1.7 , consistent with previous observations of Cen A. This component is variable by 57% on timescales of months but not on shorter timescales of kiloseconds. A single, heavily absorbed power-law model does not adequately fit the spectrum of Cen A, as at low energies (~ 2 keV) an excess is found. We have discussed two more complex models to explain the observed X-ray emission. In the first model, $\sim 90\%$ of the nucleus is covered by an absorbing column of $\sim 10^{23}$ atoms cm^{-2} , and $\sim 10\%$ remainder by an absorbing column of $\sim 4 \times 10^{22}$ atoms cm^{-2} . In the second model, we observe unresolved X-ray emission from two distinct power-law components, each with some intrinsic absorption.
3. The model with a second, less absorbed power-law component is consistent with X-ray emission produced in the subparsec-scale radio jet in Cen A. We show that the measured X-ray luminosity of the second power law component in Cen A lies on or near the trendline established for other low-power radio galaxy cores.
4. Using Bondi accretion theory, we estimate the accretion rate of gravitationally captured hot X-ray-emitting gas onto the central black hole to be $\sim 6 \times 10^{-4} M_{\odot} \text{ yr}^{-1}$. We calculate an efficiency, η_{Bondi} , by comparing the measured X-ray luminosity with the calculated Bondi luminosity. We find the upper limit of η_{Bondi} to be $\sim 0.2\%$, which is several orders of magnitude higher than other galaxies thought to have radiatively inefficient accretion flows, though smaller than the canonical efficiency for a standard disk. We favor an accretion model in the form of a standard, geometrically thin, optically thick disk, although note that there are uncertainties associated with the role that cold gas might have in the accretion process, together with the assumed value of M_{BH} .

We are grateful for support for this work from PPARC (a Studentship for D.A.E. and research grant for D.M.W.), the Royal Society (Research Fellowship for M.J.H.), and NASA (contracts NAS8-38248 and NAS8-39073 with the Smithsonian Astrophysical Observatory). D.A.E. thanks the Harvard-Smithsonian Center for Astrophysics for its hospitality. We are grateful to the Almudena Prieto and the anonymous referee for useful comments.

REFERENCES

- Baganoff, F. K., et al. 2003, ApJ, 591, 891
- Bearden, J. A. 1967, Rev. Mod. Phys., 39, 78
- Benlloch, S., Rothschild, R. E., Wilms, J., Reynolds, C. S., Heindl, W. A., & Staubert, R. 2001, Astron. Astrophys., 371, 858
- Bondi, H. 1952, MNRAS, 112, 195
- Canosa, C. M., Worrall, D. M., Hardcastle, M. J., & Birkinshaw, M. 1999, MNRAS, 310, 30
- Chiaberge, M., Capetti, A., & Celotti, A. 2001, MNRAS, 324, 33
- De Filippis, E., Schindler, S., & Castillo-Morales, A. 2003, Astron. Astrophys., 404, 63
- Dickey, J. M., & Lockman, F. J. 1990, ARA&A, 28, 215
- Di Matteo, T., Allen, S. W., Fabian, A. C., Wilson, A. S., & Young, A. J. 2003, ApJ, 582, 133
- Ehle, M., et al. 2003, *XMM-Newton* User’s Handbook, version 2.1, http://xmm.vilspa.esa.es/external/xmm_user_support/documentation/uhb/XMM_UHB.html
- Fabbiano, G., Trinchieri, G., Elvis, M., Miller, L., Longair, M. 1984, ApJ, 277, 115
- Gammie, C. F., Narayan, R., & Blandford, R. 1999, ApJ, 516, 177
- Ghizzardi, S. 2001a, “In-flight calibration of the on-axis and near off-axis PSF for the MOS1 and MOS2 cameras”, XMM-SOC-CAL-TN-0022, available from <http://www xmm.vilspa.esa.es>
- Ghizzardi, S. 2001b, “In-flight calibration of the PSF for the PN camera”, XMM-SOC-CAL-TN-0023, available from <http://www xmm.vilspa.esa.es>
- Glozzi, M., Sambruna, R. M., & Brant, W. N. 2003, A&A, 408, 949
- Glozzi, M., Sambruna, R. M., Brant, W. N., Mushotzky, R., & Eracleous, M. 2004, A&A, 413, 139
- Grandi, P., et al. 2003, ApJ, 593, 160
- Grindlay, J.E. 1975, ApJ, 199, 49

- Hardcastle, M. J., & Worrall, D. M. 1999, MNRAS, 309, 969
- Hardcastle, M. J., Birkinshaw, M., & Worrall, D. M. 2000, MNRAS, 326, 1499
- Hardcastle, M. J., Worrall, D. M., Kraft, R. P., Forman, W. R., Jones, C., & Murray, S. S. 2003 ApJ, 593, 169
- Israel, F. P. 1998, A&A Rev., 8, 237
- Karovska, M., Fabbiano, G., Nicastro, F., Elvis, M., Kraft, R. P., & Murray, S. S. 2002, ApJ, 577, 114
- Kraft, R. P., et al. 2000, ApJ, 531, L9
- Kraft, R. P., Kregenow, J. M., Forman, W. R., Jones, C., Murray, S. S. 2001, ApJ, 560, 675
- Kraft, R. P., Forman, W. R., Jones, C., Murray, S. S., Hardcastle, M. J., & Worrall, D. M. 2002, ApJ, 569, 54
- Kraft, R. P., Vázquez, S. E., Forman, W. R., Jones, C., Murray, S. S., Hardcastle, M. J., Worrall, D. M., & Churazov, E. 2003, ApJ, 592, 129
- Loewenstein, M., Mushotzky, R. F., Angelini, L., Arnaud, K. A., & Quataert, E. 2001, ApJL, 555, L24
- Marconi, A., et al. 2001, ApJ, 549, 915
- Marshall, H.L., et al. 2004, ApJ, in preparation
- Miyazaki, S., et al. 1996, Publ. Astron. Soc. Japan, 48, 801
- Molendi, S., & Sembay, S. 2003, “Assessing the EPIC Spectral Calibration in the Hard Band with a 3C273 Observation”, XMM-SOC-CAL-TN-0036, available from <http://www.xmm.vilspa.esa.es>
- Mushotzky, R. F., Serlemitsos, P. J., Boldt, E. A., Holt, S. S., & Becker, R. H. 1978, ApJ, 220, 790
- Narayan, R., & Yi, I. 1995, ApJ, 452, 710
- Narayan, R., McClintock, J. E., & Yi, I. 1996, ApJ, 457, 821
- Quataert, E. 2003, Astron. Nachr., 324, S1, Special Supplement “The central 300 parsecs of the Milky Way”, Eds. Cotera, A., Falcke, H., Geballe, T. R., Markoff, S.

- Rejkuba, M. 2004, *A&A*, 413, 903
- Reynolds, C. S., Nowak, M. A., & Maloney, P. R. 2000, *ApJ*, 540, 143
- Shakura, N. I., & Sunyaev, R. A. 1973, *A&A*, 24, 337
- Sugizaki, M., Inoue, H., Sonobe, T., Takahashi, T., & Yamamoto, Y. 1997, *PASJ*, 49, 59
- Tingay, S. J., et al. 1998, *A. J.*, 115, 960
- Tucker, W., Kellogg, E., Gursky, H., Giacconi, R., & Tananbaun, H. 1973, *ApJ*, 180, 715
- Turner, T. J., George, I. M., Nandra, K., & Mushotzky, R. F. 1997a, *ApJ*, 475, 118
- Turner, T. J., George, I. M., Nandra, K., & Mushotzky, R. F. 1997b, *ApJS*, 113, 23
- Wilson, A. S., & Yang, Y. 2002, *ApJ*, 568, 133
- Woźniak, P. R., Zdziarski, A. A., Smith, D., Madejski, G. M., & Johnson, W. N. 1998, *MNRAS*, 299, 449
- Worrall, D. M., & Birkinshaw, M. 1994, *Ap. J.*, 427, 134
- Worrall, D. M., & Birkinshaw, M. 2003, *MNRAS*, 340, 1261

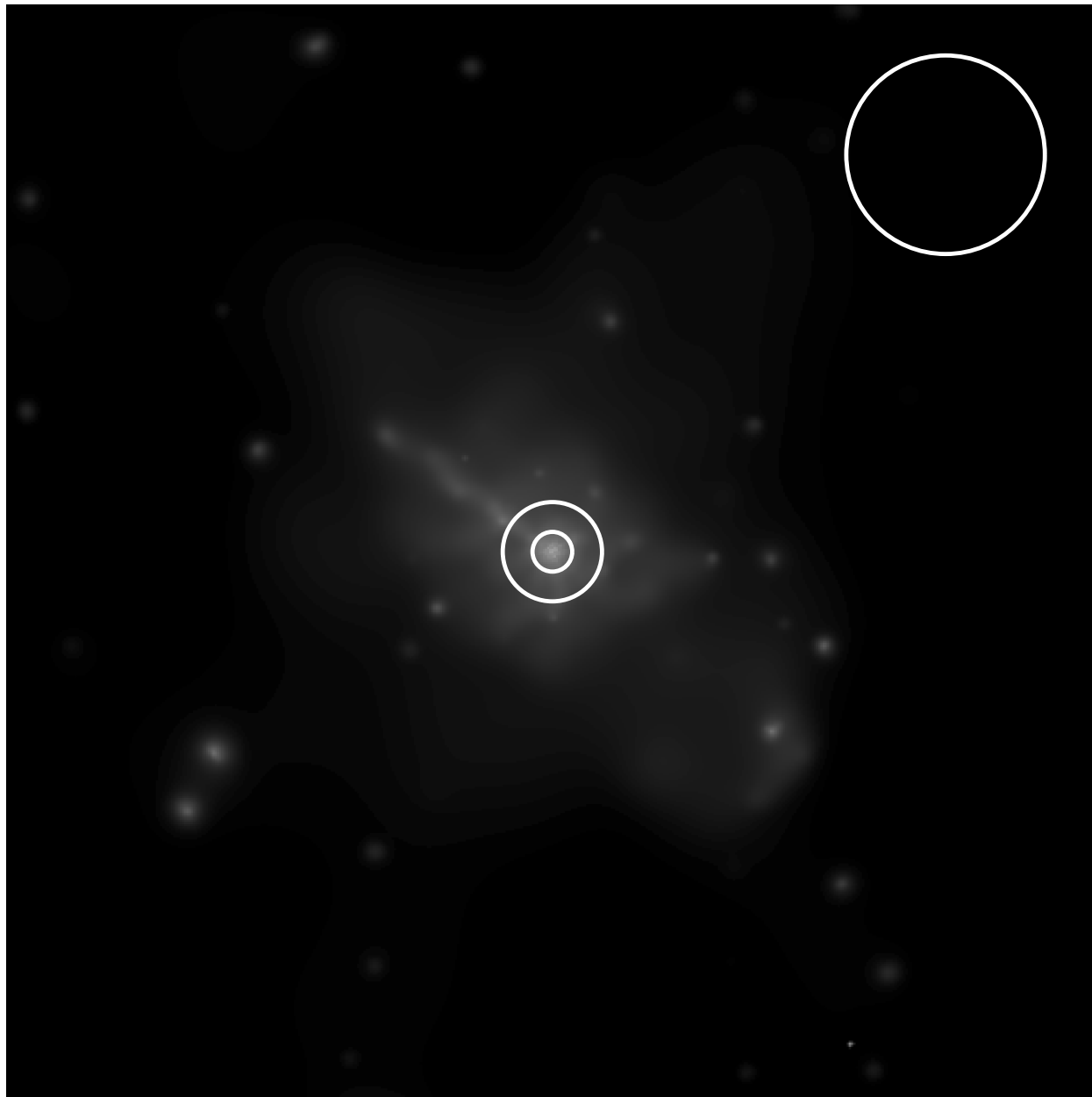


Fig. 1.— Co-added, adaptively smoothed, MOS1, MOS2, and pn image of the second *XMM-Newton* observation of Cen A. The energy band is 0.5–4 keV so that both diffuse and pointlike emission may be seen. Pattern selection is 0–4 for the MOS cameras and 0–12 for the pn. No exposure or vignetting correction has been made. A source-centered annulus of inner radius 20'' and outer radius 50'' is shown, together with a large off-source circle used for local background.

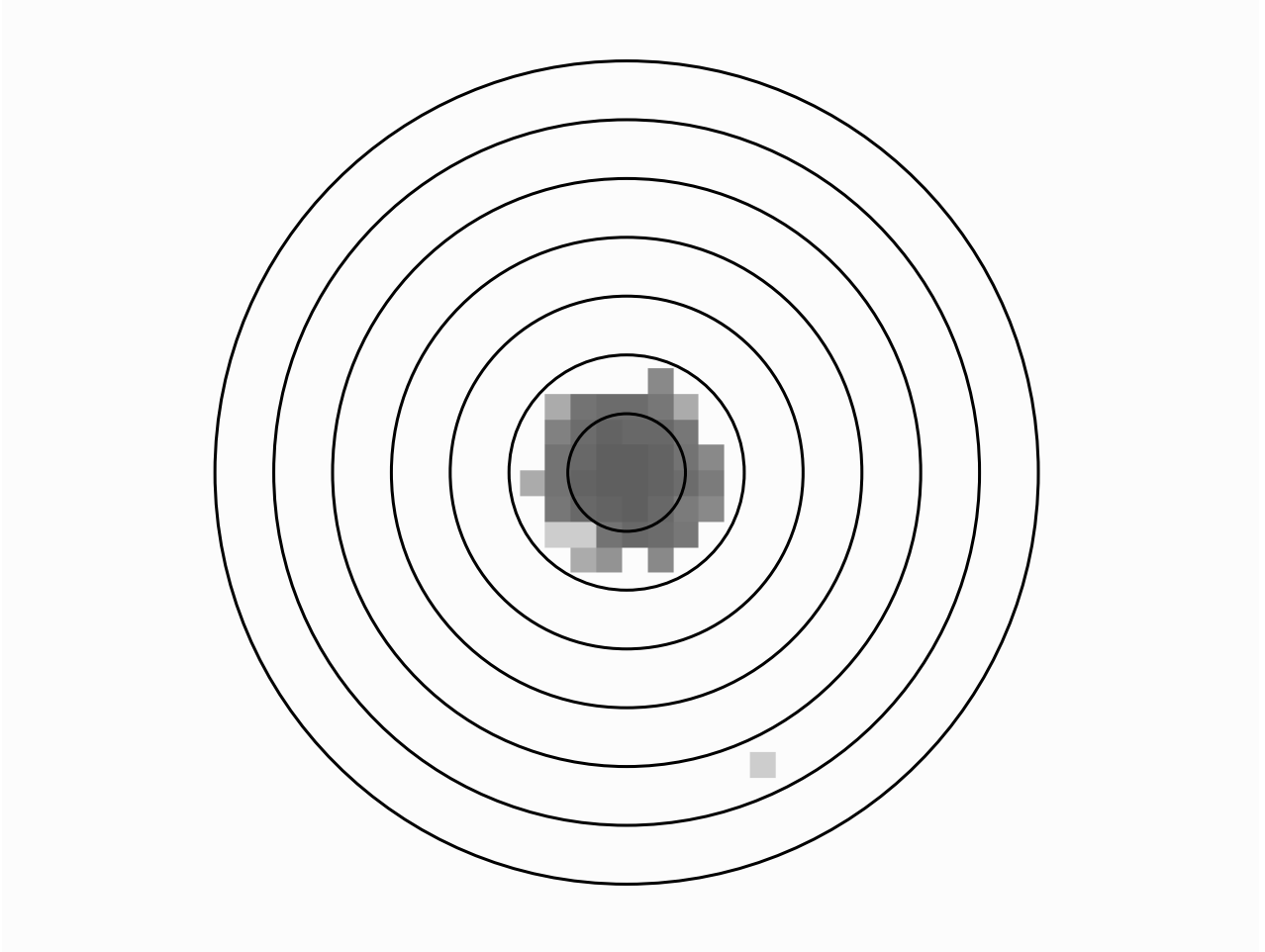


Fig. 2.— *XMM-Newton* pn image comprised of events that cannot be produced by a single photon, i.e. those predominantly produced by pileup. This is produced by selecting events with the *XMM-Newton* FLAG XMMEA_0. Concentric source-centered circles of radii $10''$ – $70''$ are shown. This shows that pileup is insignificant at distances greater than $20''$ from the center, and so motivates our choice of extraction region.

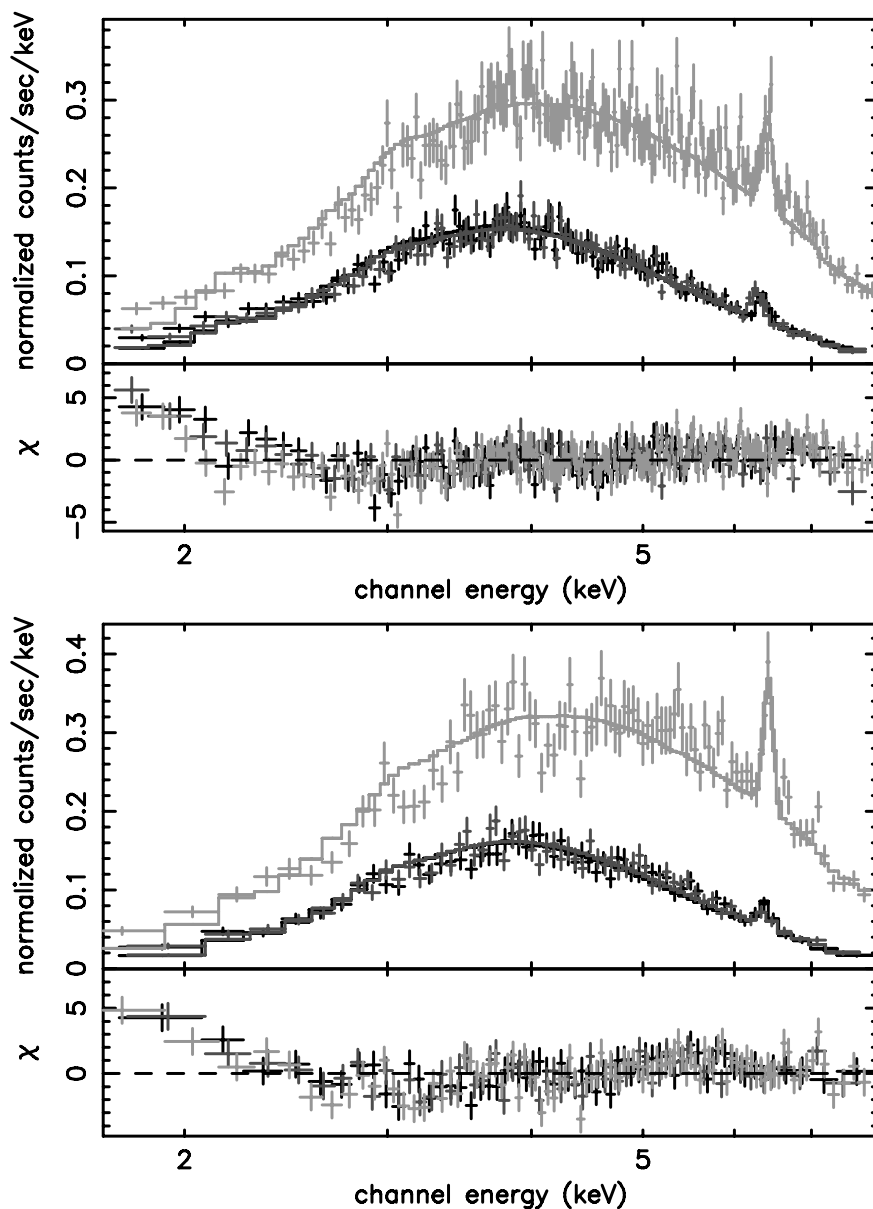


Fig. 3.— Spectral fit to data from the *XMM-Newton* observations with a single absorbed power-law model, with contributions to χ^2 shown. The top panel shows data from the first *XMM-Newton* observation, and the bottom panel data from the second *XMM-Newton* observation. The data from the MOS1, MOS2, and pn cameras are denoted, respectively, in black, dark gray, and light gray. This shows the poor fit at low energies and the need for a more complex spectral model.

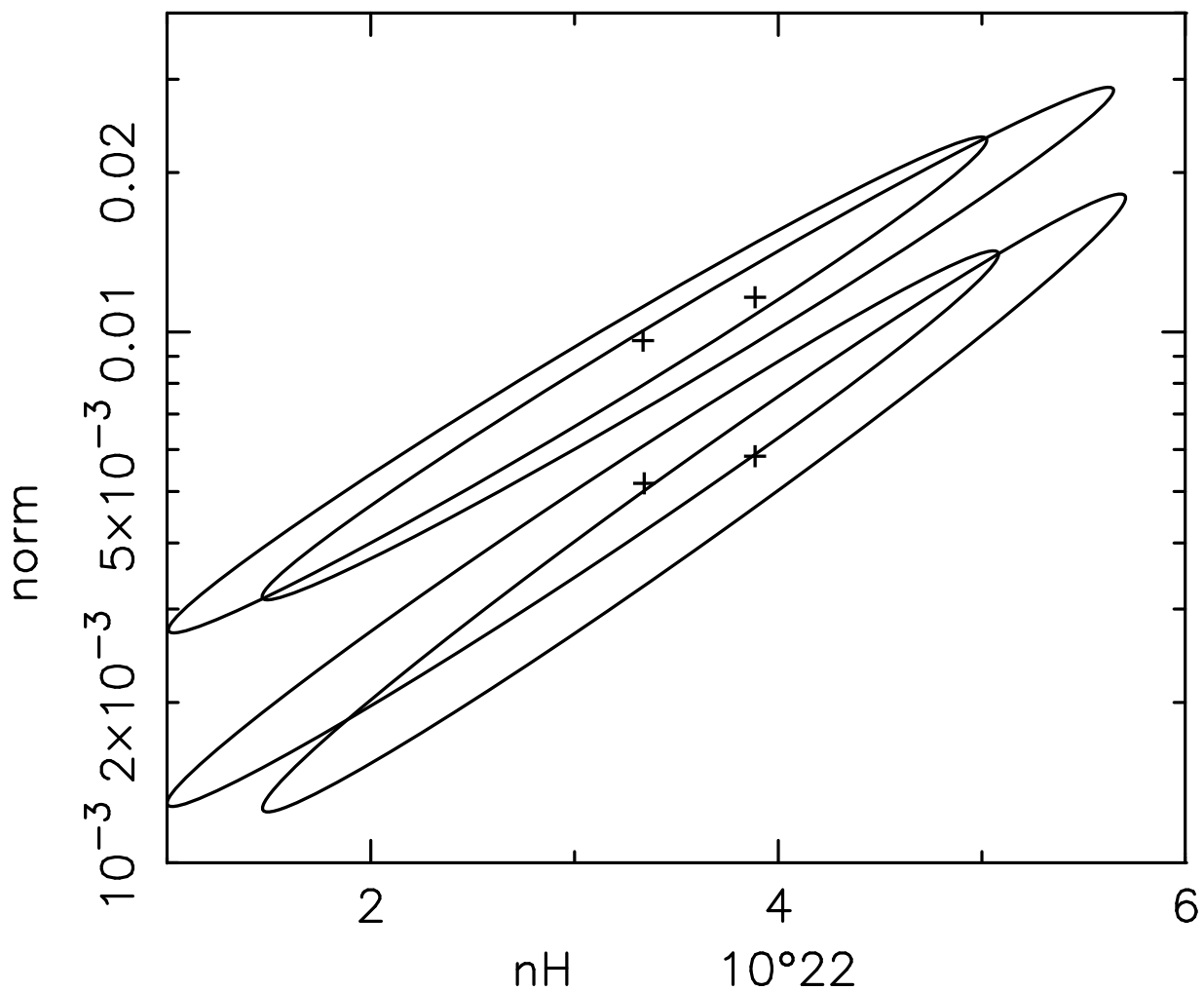


Fig. 4.— *XMM-Newton* first observation, second power-law 90% confidence contours ($\chi^2_{\min} + 4.61$) for MOS1 (*top two*) and pn (*bottom two*). The confidence contours shown for each camera correspond to 90% confidence upper and lower flux limits for the contribution of jet and gas emission in the annulus, as modeled using the *Chandra* ACIS CCD's. The disagreement in normalization between the MOS and pn cameras is discussed in the text.

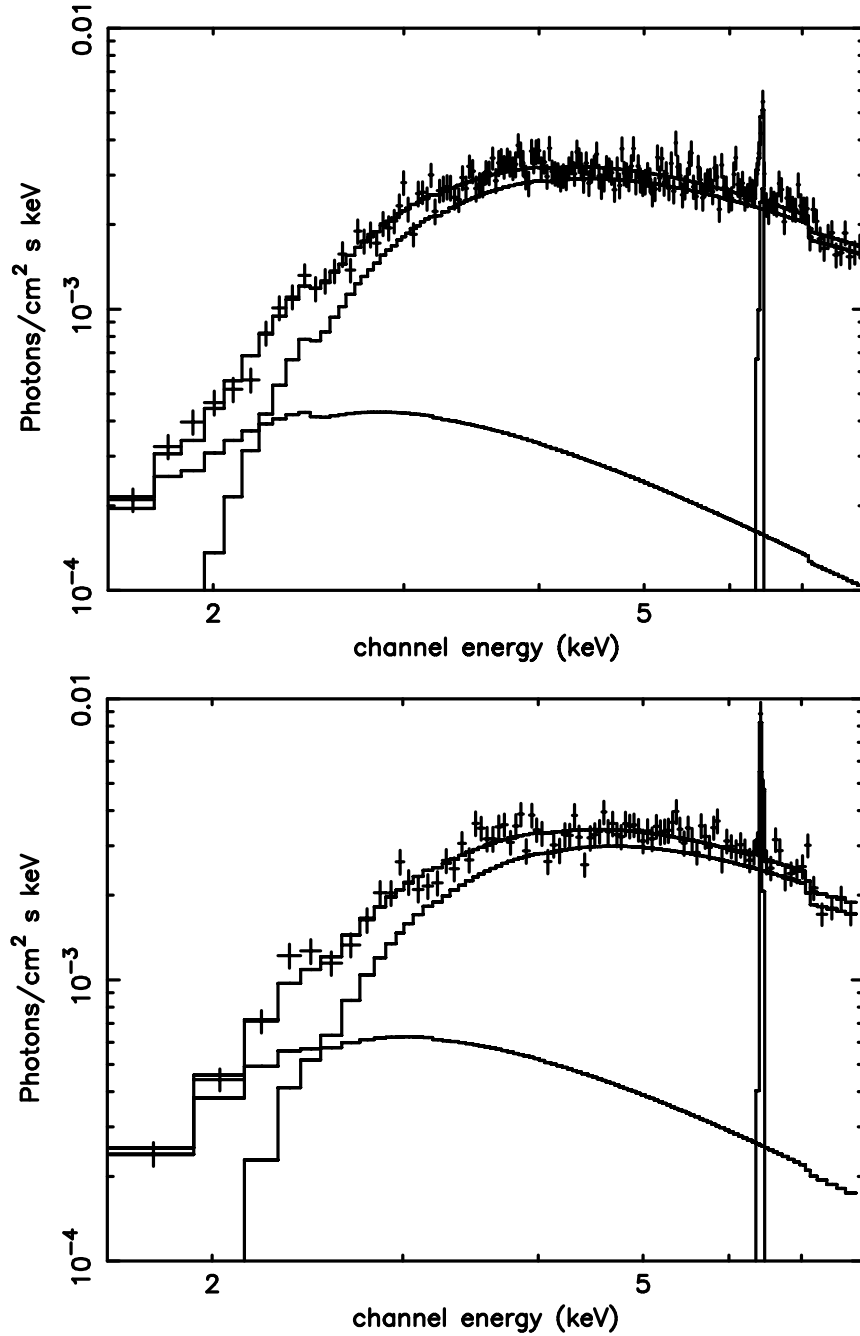


Fig. 5.— Unfolded spectrum for the two *XMM-Newton* observations showing the model fit to two absorbed power laws and an Fe K α line. The upper panel shows data from the first *XMM-Newton* observation, and the lower panel data from the second *XMM-Newton* observation. For clarity, only the pn data are shown.

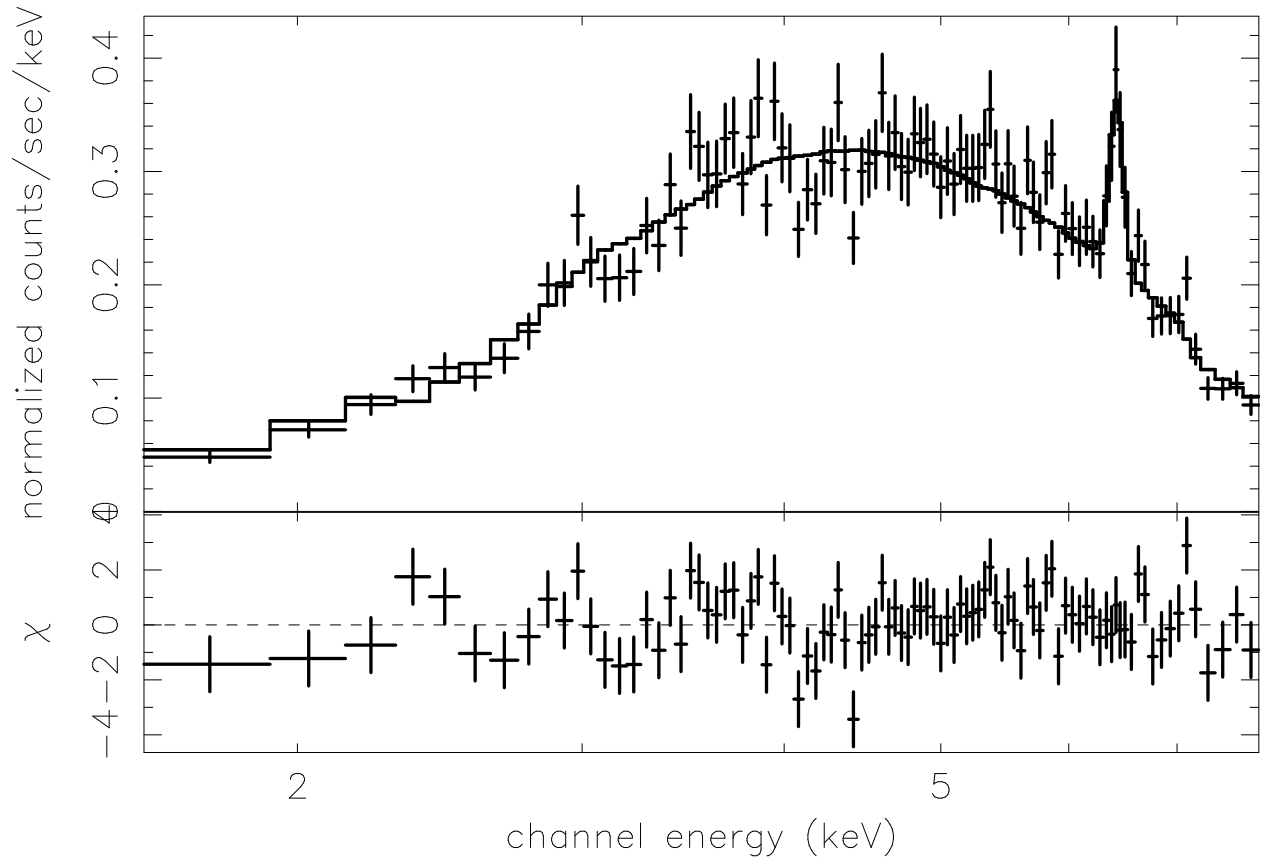


Fig. 6.— The pn counts spectrum for the second *XMM-Newton* observation showing the model fit to a partially-covered absorber with one power-law and an Fe $K\alpha$ line. This model provides an adequate description of the observed low energy emission.

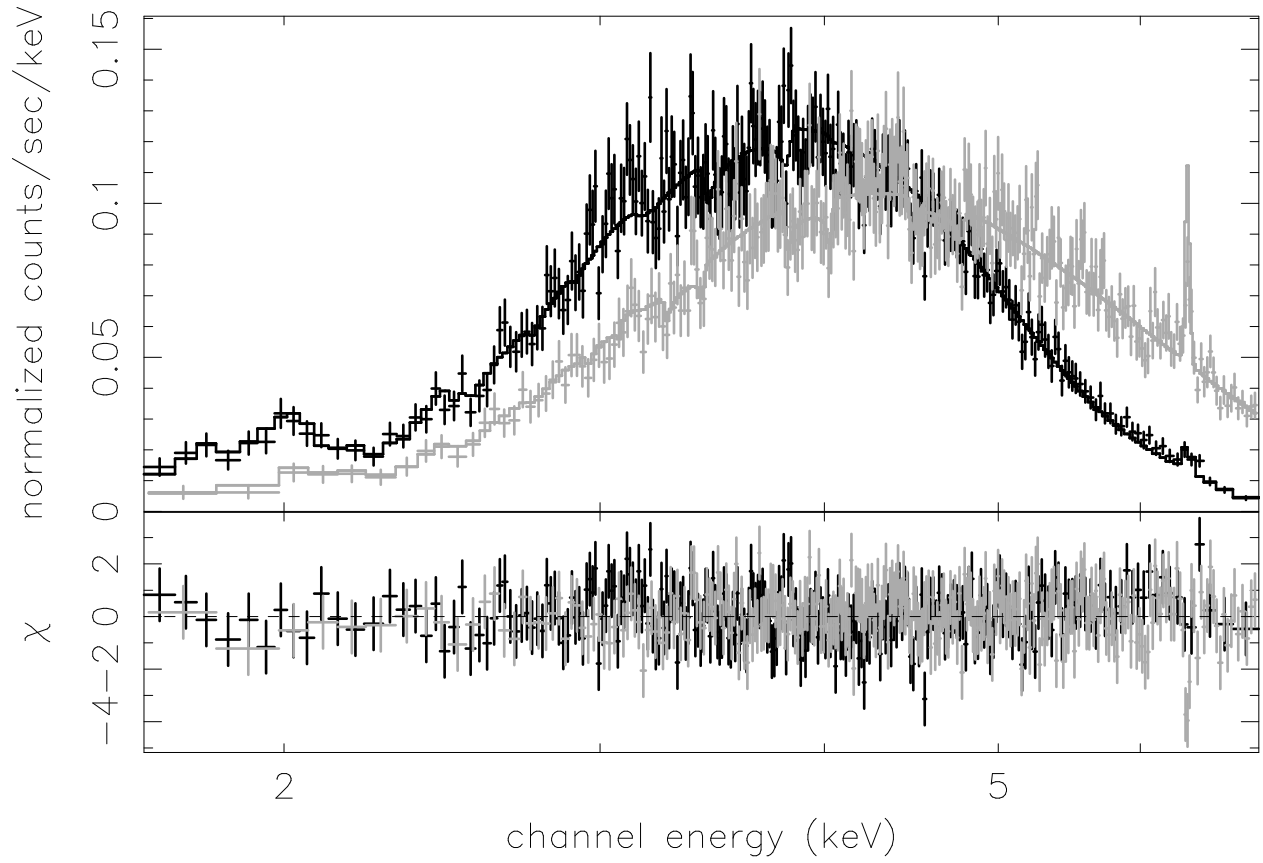


Fig. 7.— *Chandra* counts spectrum showing the model fit to two absorbed power-laws and an Fe $K\alpha$ line. The MEG-1 data and model are denoted by in black and the HEG-1 data and model in light gray.

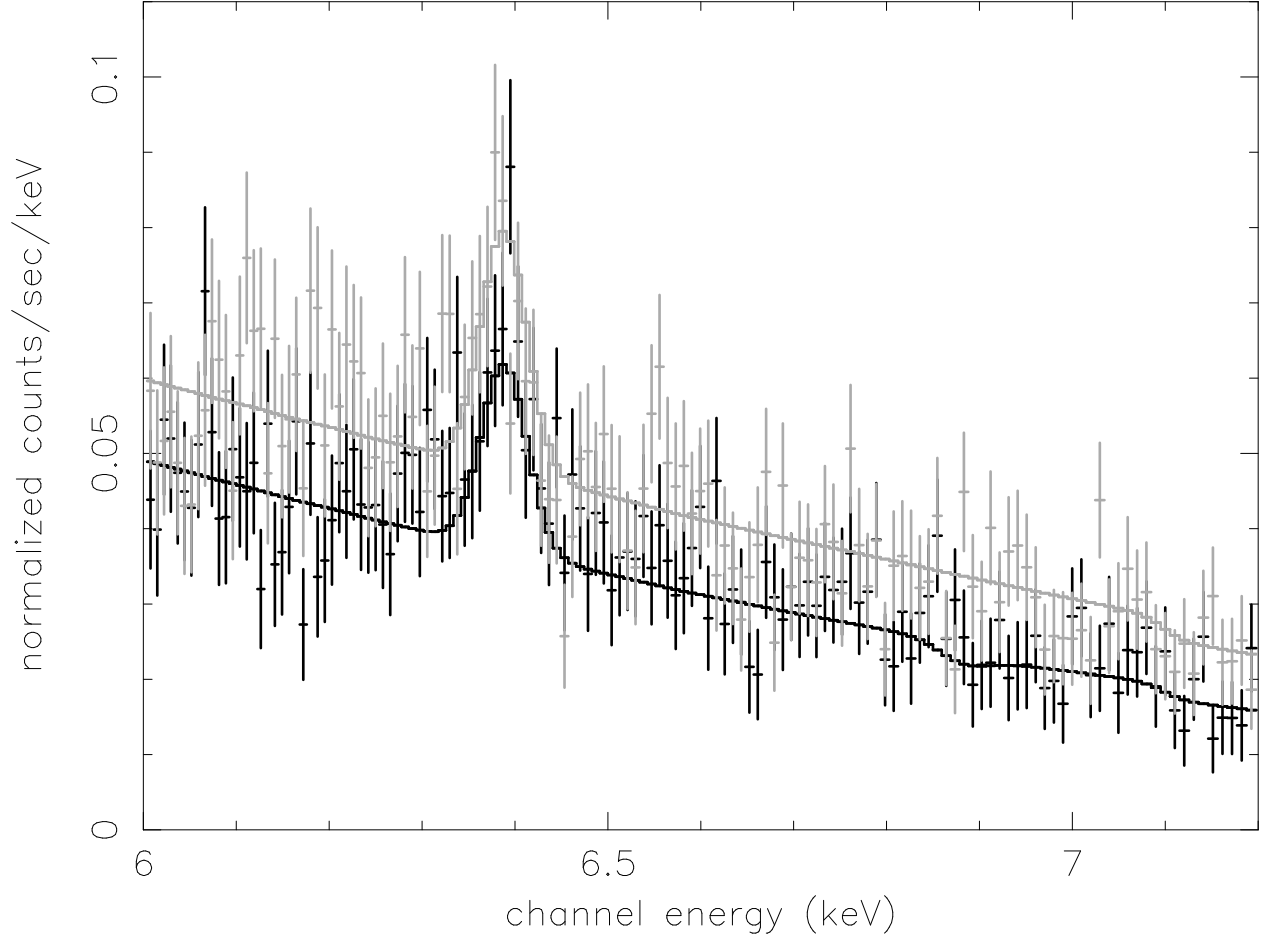


Fig. 8.— The 6.0–7.2 keV counts spectrum for the *Chandra* HEG+1 (*black*) and HEG-1 (*light gray*) observations, showing the model fit to Fe $K\alpha$ line emission, modelled as a doublet, and the nuclear continuum. The Fe $K\alpha$ lines were found to be broadened, with a line width ~ 20 eV.

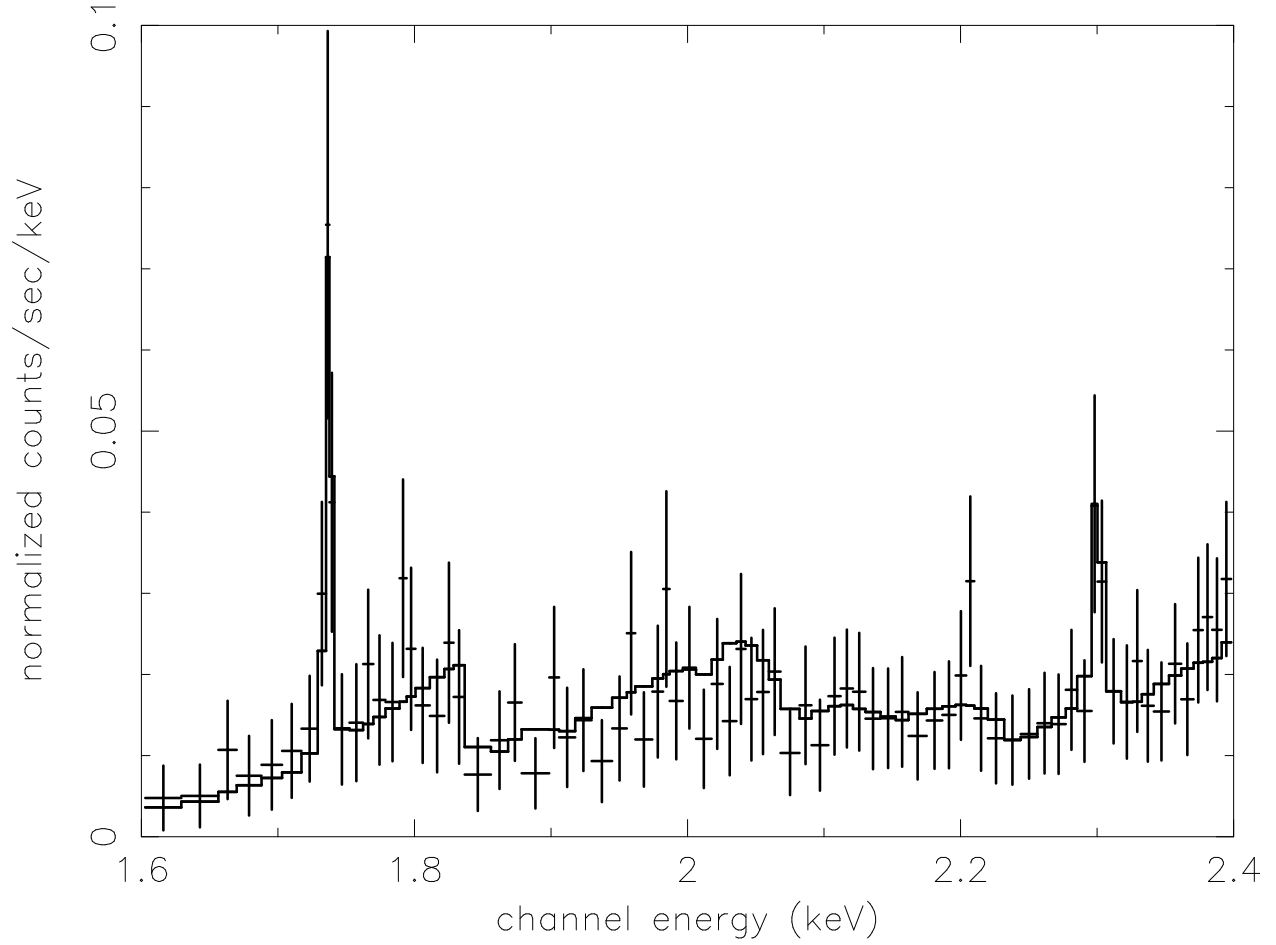


Fig. 9.— The 1.6–2.4 keV counts spectrum for the *Chandra* MEG-1 observation, showing unresolved $K\alpha$ emission lines from neutral Si at 1.74 keV, neutral S at 2.30 keV, and the nuclear continuum.

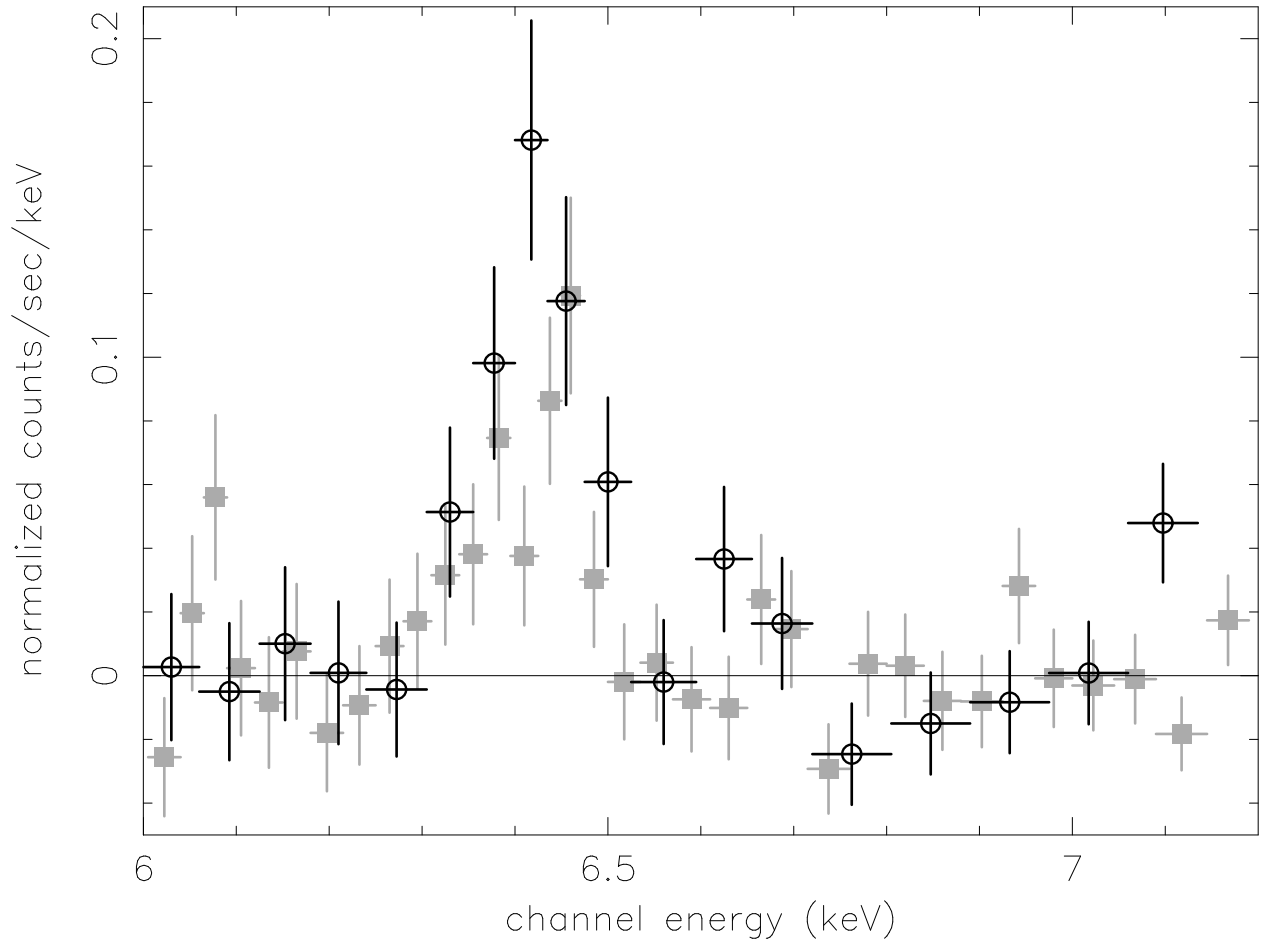


Fig. 10.— 6.0–7.2 keV residuals for the *XMM-Newton* pn observations, after fitting the nuclear spectrum to a hard, heavily-absorbed power-law. The first observation is represented by gray squares and the second by black circles. Emission from Fe $K\alpha$ at 6.4 keV is clearly apparent.

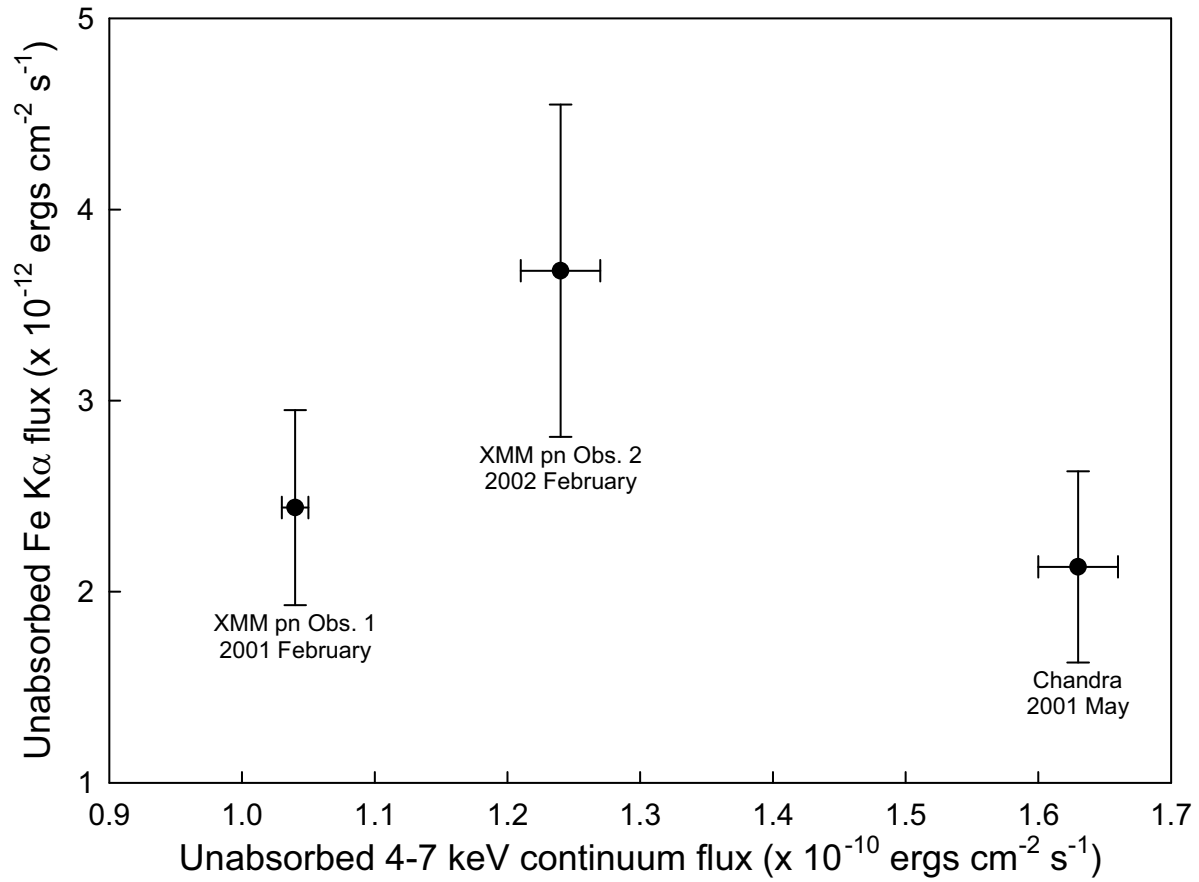


Fig. 11.— Unabsorbed Fe K α line flux vs. unabsorbed 4–7 keV continuum flux for the two *XMM-Newton* observations (pn camera only), and the *Chandra* HETGS observation, with 90% confidence errors shown. This shows the lack of response of the Fe K α line to changes in the continuum flux.

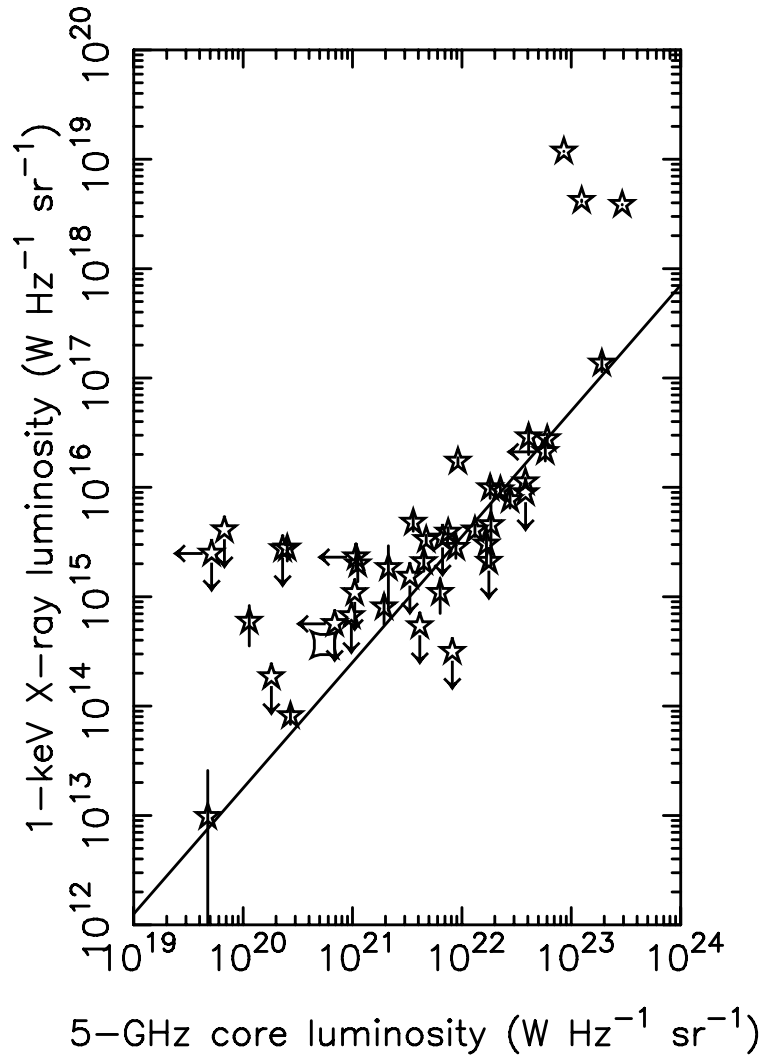


Fig. 12.— Soft X-ray luminosity (as measured with *ROSAT*) plotted against 5 GHz radio core luminosity for the B2 sample of radio galaxies (*stars*; see Canosa et al. 1999 for a full explanation), and Cen A (*squashed box*). This shows that the Cen A lies near the previously established trendline (solid line) for the B2 galaxies.

Table 1. *XMM-Newton* and *Chandra* best fit continuum spectral parameters with a two power-law model

Observation	Component	Parameters	1 keV normalization (photons cm ⁻² s ⁻¹ keV ⁻¹)
<i>XMM-Newton</i> 1	1st Power Law	$N_{\text{H}} = (1.19 \pm 0.13) \times 10^{23}$ atoms cm ⁻² $\Gamma = 1.74^{+0.11}_{-0.09}$...	MOS1 = $(9.36 \pm 1.51) \times 10^{-2}$ MOS2 = $(8.39 \pm 1.34) \times 10^{-2}$ pn = $(7.32 \pm 1.25) \times 10^{-2}$
	2nd Power Law	$N_{\text{H}} \simeq (3.6^{+2.2}_{-2.3}) \times 10^{22}$ atoms cm ⁻² $\Gamma = 2$ (fixed) ...	MOS1 = $(9.52^{+13.40}_{-6.63}) \times 10^{-3}$ MOS2 = $(9.98^{+13.74}_{-6.96}) \times 10^{-3}$ pn = $(5.40^{+7.66}_{-4.17}) \times 10^{-3}$
<i>Chandra</i> HETGS	1st Power Law	$N_{\text{H}} = (1.00 \pm 0.06) \times 10^{23}$ atoms cm ⁻² $\Gamma = 1.64 \pm 0.07$...	$(9.65 \pm 1.41) \times 10^{-2}$...
	2nd Power Law	$N_{\text{H}} = 3.8 \times 10^{22}$ atoms cm ⁻² (fixed) $\Gamma = 2$ (fixed) ...	$(1.74^{+1.46}_{-1.45}) \times 10^{-3}$...
<i>XMM-Newton</i> 2	1st Power Law	$N_{\text{H}} = (1.40 \pm 0.20) \times 10^{23}$ atoms cm ⁻² $\Gamma = 1.77^{+0.19}_{-0.15}$...	MOS1 = $(10.39 \pm 3.13) \times 10^{-2}$ MOS2 = $(9.79 \pm 2.90) \times 10^{-2}$ pn = $(8.35 \pm 2.60) \times 10^{-2}$
	2nd Power Law	$N_{\text{H}} \simeq (4.0^{+1.8}_{-1.6}) \times 10^{22}$ atoms cm ⁻² $\Gamma = 2$ (fixed) ...	MOS1 = $(11.10^{+8.51}_{-5.12}) \times 10^{-3}$ MOS2 = $(11.29^{+8.81}_{-5.33}) \times 10^{-3}$ pn = $(6.04^{+6.52}_{-3.18}) \times 10^{-3}$

Note. — Uncertainties are 90% for one interesting parameter (i.e., $\chi^2_{\text{min}} + 2.7$).

Table 2. *XMM-Newton* best fit continuum spectral parameters for a partial covering model

Observation	Joint parameters	1 keV normalization (photons cm ⁻² s ⁻¹ keV ⁻¹)
<i>XMM-Newton</i> 1	$N_{\text{H},1} = (4.28^{+0.93}_{-1.18}) \times 10^{22}$ atoms cm ⁻²	MOS1 = $(9.67^{+2.10}_{-1.75}) \times 10^{-2}$
	$N_{\text{H},2} = (7.53^{+0.65}_{-0.57}) \times 10^{22}$ atoms cm ⁻²	MOS2 = $(8.92^{+1.93}_{-1.61}) \times 10^{-2}$
	$\Gamma = 1.72 \pm 0.10$	pn = $(7.21^{+1.56}_{-1.32}) \times 10^{-2}$
	Covering fraction = $0.89^{+0.05}_{-0.07}$...
<i>XMM-Newton</i> 2	$N_{\text{H},1} = (4.54^{+0.65}_{-1.75}) \times 10^{22}$ atoms cm ⁻²	MOS1 = $(10.73^{+4.40}_{-3.04}) \times 10^{-2}$
	$N_{\text{H},2} = (8.81^{+1.48}_{-0.90}) \times 10^{22}$ atoms cm ⁻²	MOS2 = $(10.30^{+4.21}_{-2.91}) \times 10^{-2}$
	$\Gamma = 1.73 \pm 0.17$	pn = $(8.34^{+3.42}_{-2.37}) \times 10^{-2}$
	Covering fraction = $0.89^{+0.05}_{-0.07}$...

Note. — Uncertainties are 90% for one interesting parameter (i.e., $\chi^2_{\text{min}} + 2.7$).

Table 3. Emission line parameters

Line	Observation	Centroid (keV)	Line width (eV)	Equivalent width (eV)	Unabsorbed flux ($\times 10^{-12}$ ergs cm $^{-2}$ s $^{-1}$)
Fe K α	<i>XMM-Newton</i> 1	$6.417^{+0.034}_{-0.009}$	10 (fixed)	$81.6^{+33.4}_{-33}$	$2.44^{+0.52}_{-0.49}$
	<i>Chandra</i> HETGS	$K\alpha_1 = 6.404 \pm 0.006$	$20^{+8.99}_{-8.11}$	$43.6^{+18.0}_{-18.7}$	2.13 ± 0.50
		$K\alpha_2 = 6.398$
	<i>XMM-Newton</i> 2	$6.428^{+0.027}_{-0.015}$	10 (fixed)	$99.9^{+35.1}_{-52.9}$	$3.68^{+0.87}_{-0.86}$
Si K α	<i>Chandra</i> HETGS	1.740 ± 0.014	10 (fixed)	$32.7^{+6.7}_{-4.1}$	2.42 ± 0.97
S K α	<i>Chandra</i> HETGS	2.304 ± 0.024	10 (fixed)	< 10	< 0.77

Note. — The *XMM-Newton* line widths for the Fe K α line, and the *Chandra* line widths for the Si K α line and S K α lines were fixed at 10 eV (i.e., unresolved). The equivalent widths were measured relative to the primary continuum. Uncertainties are 90% for one interesting parameter (i.e., $\chi^2_{\min} + 2.7$).

Table 4. *XMM-Newton* and *Chandra* absorbed and unabsorbed 4–7 keV fluxes, and 2–10 keV unabsorbed luminosities

Observation	4–7 keV absorbed flux ($\times 10^{-10}$ ergs cm $^{-2}$ s $^{-1}$)	4–7 keV unabsorbed flux ($\times 10^{-10}$ ergs cm $^{-2}$ s $^{-1}$)	2–10 keV unabsorbed luminosity ($\times 10^{41}$ ergs s $^{-1}$)
<i>XMM-Newton</i> pn 1 (2001 February)	0.75 ± 0.01	1.04 ± 0.01	3.88 ± 0.07
<i>Chandra</i> HEG+1 (2001 May)	1.19 ± 0.03	1.63 ± 0.03	6.25 ± 0.19
<i>XMM-Newton</i> pn 2 (2002 February)	0.84 ± 0.02	1.24 ± 0.03	4.28 ± 0.12

Note. — Uncertainties are 90% for one interesting parameter (i.e., $\chi^2_{\min} + 2.7$).

Table 5. X-ray and radio flux densities and ratios for the kiloparsec-scale and parsec-scale jets

Component	1 keV X-ray flux density (μJy)	Radio flux density (Jy) (frequency)	Ratio ($\times 10^{-7}$)
kiloparsec-scale jet	0.22 ± 0.01	0.74 ± 0.12 (8.4 GHz)	3.0 ± 0.6
2nd power law / parsec-scale jet	3.31	5 (4.8 GHz)	6.6

Note. — Uncertainties are 90% for one interesting parameter (i.e., $\chi^2_{\text{min}} + 2.7$).

Table 6. Calculation of efficiencies, η_{Bondi} , by comparing the measured X-ray luminosity with the expected Bondi luminosity

Galaxy	Distance (Mpc)	M_{SMBH} (M_{\odot})	\dot{M}_{Bondi} ($M_{\odot} \text{ yr}^{-1}$)	L_{Edd} (ergs s^{-1})	$\dot{M}_{Bondi}c^2$ (ergs s^{-1})	L_X (ergs s^{-1})	Energy range (keV)	η_{Bondi}	Ref	Interpretation
Milky Way	8.0×10^{-3}	2.6×10^6	1.0×10^{-5}	3.3×10^{44}	1.0×10^{42}	2.4×10^{33}	2–10	2.4×10^{-9}	1,2	Inefficient
Cen A	3.4	2.0×10^8	6.4×10^{-4}	2.6×10^{46}	2.1×10^{44}	4.8×10^{41}	2–10	2.3×10^{-3}	3	Standard
NGC 4636	15.0	7.9×10^7	8.0×10^{-5}	1.0×10^{46}	4.5×10^{42}	2.7×10^{38}	2–10	6.0×10^{-5}	4	Inefficient
NGC 4472	16.7	5.7×10^8	7.9×10^{-3}	7.2×10^{46}	4.5×10^{44}	6.4×10^{38}	2–10	1.4×10^{-6}	5	Inefficient
M87	18.0	3.0×10^9	1.0×10^{-1}	3.8×10^{47}	5.0×10^{45}	7.0×10^{40}	0.5–7	1.4×10^{-5}	5	Inefficient
NGC 1399	20.5	1.1×10^9	4.0×10^{-2}	1.4×10^{47}	2.3×10^{45}	9.7×10^{38}	2–10	4.2×10^{-7}	4	Inefficient
NGC 4261	31.6	4.9×10^8	4.5×10^{-2}	6.2×10^{46}	2.5×10^{45}	1.2×10^{41}	0.3–10	4.8×10^{-5}	6	Inefficient
NGC 6251	94.4	6.0×10^8	8.0×10^{-3}	7.6×10^{46}	4.6×10^{44}	8.8×10^{42}	0.4–10	1.9×10^{-2}	7	Standard

References. — (1) Quataert 2003; (2) Baganoff et al. 2003; (3) Present work; (4) Loewenstein et al. 2001; (5) Di Matteo et al. 2003; (6) Gliozzi et al. 2003; (7) Gliozzi et al. 2004